nature physics

ARTICLES

https://doi.org/10.1038/s41567-021-01376-z

Check for updates

Evidence of topological boundary modes with topological nodal-point superconductivity

Abhay Kumar Nayak[1,5], Aviram Steinbok[1,5], Yotam Roet[1,5], Jahyun Koo[1], Gilad Margalit[1], Irena Feldman[2], Avior Almoalem[2], Amit Kanigel[2], Gregory A. Fiete[3,4], Binghai Yan[1], Yuval Oreg[1], Nurit Avraham[1]✉ and Haim Beidenkopf[1]✉

Topological superconductors are an essential component for topologically protected quantum computation and information processing. Although signatures of topological superconductivity have been reported in heterostructures, material realizations of intrinsic topological superconductors are rather rare. Here we use scanning tunnelling spectroscopy to study the transition metal dichalcogenide 4Hb-TaS_2 that interleaves superconducting 1H-TaS_2 layers with strongly correlated 1T-TaS_2 layers, and find spectroscopic evidence for the existence of topological surface superconductivity. These include edge modes running along the 1H-layer terminations as well as under the 1T-layer terminations, where they separate between superconducting regions of distinct topological nature. We also observe signatures of zero-bias states in vortex cores. All the boundary modes exhibit crystallographic anisotropy, which—together with a finite in-gap density of states throughout the 1H layers—allude to the presence of a topological nodal-point superconducting state. Our theoretical modelling attributes this phenomenology to an inter-orbital pairing channel that necessitates the combination of surface mirror symmetry breaking and strong interactions. It, thus, suggests a topological superconducting state realized in a natural compound.

Topological superconductors are extensively explored with the aim to induce and manipulate Majorana zero modes that are essential to realize topological quantum information processing. The non-local nature of these zero modes and their intrinsic non-Abelian braiding statistics allow for quantum information to be stored and manipulated in a non-local manner, which protects it from the influence of the local environment[1,2]. A growing body of realizations of topological superconductors in one-dimensional (1D) systems have been reported so far, including hybrid nanowires[3], atomic chains[4], proximitized helical edge modes[5] and planar Josephson junctions[6,7]. In these systems, Majorana zero modes manifest themselves as zero-energy conductance anomalies localized at the ends of the topological superconducting segment. In two-dimensional (2D) systems, Majorana zero modes may be manifested as zero-bias conductance (ZBC) peaks at the centre of vortex cores[8–12]. A complementary hallmark of a 2D topological superconductor is the existence of gapless Majorana edge modes bound to its 1D boundaries[13–15]. These could be the physical boundaries of the system or separate superconducting regions with distinct topological nature. So far, signatures of 1D Majorana edge modes have been mostly observed in heterostructures or hybrid systems[16–18], in which topological superconductivity emerges from the interplay of magnetism, superconductivity and spin–orbit coupling that are provided by the different device components. To date, evidence for topological superconductivity in naturally occurring materials has been scarce[19,20].

Transition metal dichalcogenides (TMDs) are strongly correlated materials exhibiting numerous different intriguing phases such as superconductivity, charge-density-wave (CDW) order and spin liquid state[21–25]. The combination of strong spin–orbit interactions and strong electron interactions renders them to be an ideal hunting ground for topological superconductivity[26–34]. Their van der Waals nature further allows one to mix and match various materials with diverse phenomenologies either in growth or via exfoliation and stacking[35]. We use scanning tunnelling microscopy (STM) and scanning tunnelling spectroscopy to study the superconducting state in TMD 4Hb-TaS_2, which comprises the alternating stacking of 1T-TaS_2 and 1H-TaS_2 layers (Fig. 1a). While bulk 1T-TaS_2 is expected to host a quantum spin liquid state[36], bulk 2H-TaS_2 is well known for its quasi-2D Ising superconductivity[23]. Furthermore, the observation of increased muon spin rotation concurrently rising with the superconducting state of 4Hb-TaS_2 has raised the possibility of non-trivial topology[37]. Our measurements reveal the presence of 1D boundary edge modes as well as ZBC peaks at the vortex cores. These have the phenomenology of a nodal-point topological superconductor[34] stemming from inter-orbital Cooper pairing[14,38–40].

Results

We cleave single crystals along the [001] orientation under an ultra-high vacuum. Due to the alternating layer structure of 4Hb-TaS_2, the cleave exposes sulfur surfaces of both 1T and 1H terminations, as well as the step edges among them[41–43], as shown in Fig. 1b. The two layer terminations can be distinguished by their characteristic CDW patterns: the 1T layers host a strong $\sqrt{13} \times \sqrt{13}$ CDW reconstruction pattern in which 13 tantalum atoms bunch in a Star-of-David formation that is arranged in a triangular superlattice, as topographically shown in Fig. 1b,c. The 1H layers host a weak intrinsic 3×3 CDW superlattice, superimposed with a strong imprint of the $\sqrt{13} \times \sqrt{13}$ CDW superlattice of the adjacent 1T layers (Fig. 1d and Supplementary Fig. 1)[44]. The native 1T CDWs on the 1T layer and their imprint on the 1H layer appear commensurate across the step edges (Fig. 1b, green lines). The different types of

[1]Department of Condensed Matter Physics, Weizmann Institute of Science, Rehovot, Israel. [2]Department of Physics, Technion–Israel Institute of Technology, Haifa, Israel. [3]Department of Physics, Northeastern University, Boston, MA, USA. [4]Department of Physics, Massachusetts Institute of Technology, Cambridge, MA, USA. [5]These authors contributed equally: Abhay Kumar Nayak, Aviram Steinbok, Yotam Roet. ✉e-mail: nurit.avraham@weizmann.ac.il; haim.beidenkopf@weizmann.ac.il

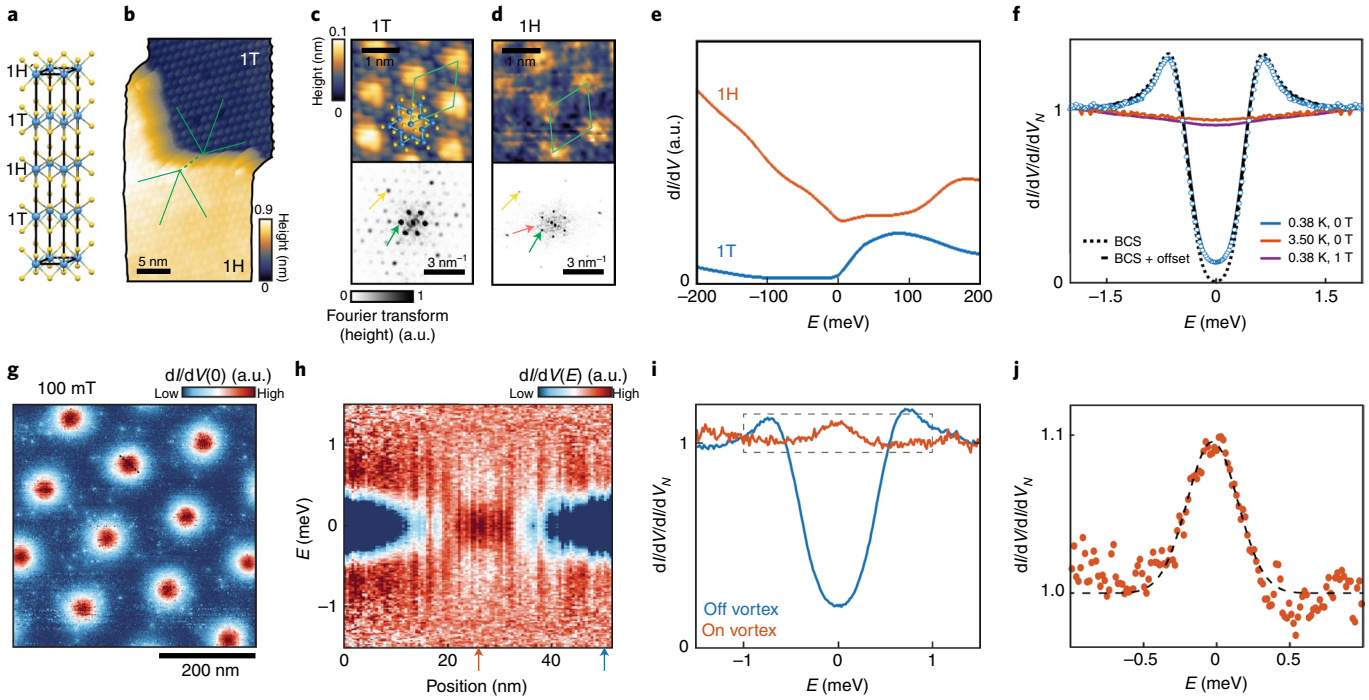

Fig. 1 | CDW, superconductivity and ZBC peaks in vortex cores. a, Crystal structure of 4Hb-TaS_2. **b**, Topography of a cleaved surface showing both 1H and 1T terminations along with their commensurate CDW patterns. **c**,**d**, Zoomed-in topography of the 1T (**c**) and 1H (**d**) terminations (top) and their corresponding Fourier transforms (bottom). The Ta and S atoms are overlaid on the topography along with the CDW unit cell (green rhombus). The Fourier transform clearly shows the atomic Bragg peak (yellow), the 1T CDW peak (green) and the 1H CDW peak (pink). **e**, Spatially averaged d*I*/d*V* in arbitrary units (a.u.) measured on the 1T and 1H terminations at 4.2 K. **f**, The d*I*/d*V* spectrum normalized by its value above the gap dI/dV_N (blue dots) measured on the 1H termination at temperature $T = 0.38$ K showing the superconducting gap fitted with a BCS spectrum and an offset BCS spectrum (dotted and solid lines, respectively). The gap vanishes above the superconducting critical temperature, T_c, and critical field, H_{c2} (orange and purple dots, respectively). **g**, Spatial mapping of ZBC in d*I*/d*V* on the 1H termination with a 100 mT out-of-plane magnetic field shows an ordered Abrikosov vortex lattice. **h**, The energy dependent spectrum, d*I*/d*V*(E) at a linecut across the vortex marked by the dashed line in **g** shows enhanced the zero-bias DOS at the core. **i**, The d*I*/d*V* profiles at the vortex core (red) and far from it (blue). The corresponding locations are marked by red and blue arrows in **h**. **j**, Zoomed-in view of the shaded box marked in **i**, showing a zero-bias peak fitted to a single Gaussian profile including instrumental broadening.

CDWs give rise to distinct Bragg peaks in the Fourier-transformed topographic images (Fig. 1c,d, bottom). The 1T and 1H terminations also differ in their surface density of states (DOS) measured in differential conductance (dI/dV), as shown in Fig. 1e. While the 1T spectrum shows low DOS around the Fermi energy and at negative biases, the 1H spectrum is metallic.

We first explore the superconducting state that forms at low temperatures in the metallic 1H layer. The spectra measured on the 1H layer at 4.2 K and at a low temperature of 380 mK are shown in Fig. 1f. A clear superconducting gap structure with accompanying coherence peaks is observed (blue circles). However, as shown in Supplementary Fig. 4, the observed gap is soft with a residual in-gap DOS, which cannot be fitted with instrumental and thermal broadening of a Bardeen–Cooper–Schrieffer (BCS) spectrum (dotted line) or by a Dynes gap profile. We obtain a tight fit by adding a finite DOS offset to a BCS gap profile (Supplementary Fig. 4, solid line), yielding a gap of $\Delta = 0.44$ meV. The superconducting gap vanishes at temperatures above 2.7 K and at out-of-plane magnetic fields higher than 0.9 T (Supplementary Fig. 3e,f and Fig. 1f, respectively), in agreement with previously reported bulk transport results[37].

At magnetic fields lower than the critical one (100 mT map is shown in Fig. 1g; additional details are provided in Supplementary Figs. 6 and 7), we image the normal vortex cores in ZBC dI/dV maps. The core DOS exponentially decays over a coherence length of $\xi \approx 21$ nm (Supplementary Fig. 6a), in agreement with values estimated from $H_{c2} \approx \Phi_o \pi \xi^2$, where Φ_o is a flux quantum. It also agrees with the value calculated from the reported Fermi velocity, namely, $v_F \approx 7 \times 10^4$ m s^{-1} (ref. [45]), together with the experimentally obtained superconducting gap ($\Delta = 0.44$ meV), which yield $\xi \approx \hbar v_F/\Delta = 29$ nm, where $\hbar$ is the Planck's constant. Note, however, that here we have used the renormalized Fermi velocity in the vicinity of the Fermi energy due to electron–phonon interactions, rather than its bare value found away from the Fermi energy and in ab initio calculations. The vortex cores are slightly anisotropic (Supplementary Fig. 3h–j). The vortices form a regular Abrikosov lattice, signifying weak pinning even though weak local fluctuations in ZBC are observed (Supplementary Fig. 5).

Careful inspection of the dI/dV spectra at the vortex cores reveals a ZBC peak localized at their centres, as shown in Fig. 1h (Supplementary Figs. 6 and 7). Representative dI/dV spectra measured on the vortex core and away from it are given in Fig. 1i, along with a magnified image of the ZBC peak at the vortex centre (Fig. 1j). A Gaussian fit finds an energy width of $\sigma = 0.25$ meV, which corresponds to a temperature scale of about 1.7 K; this is somewhat higher than the electronic temperature in our system, which is of the order of 1 K (ref. [46]) (Supplementary Fig. 4). Similar ZBC peaks at the vortex cores, identified in other electronic systems, have been attributed to topological Majorana states[8–12]. In TaS_2, however, the small energy-level spacing between the Caroli–de Gennes–Matricon core states ($\delta \approx \Delta^2/E_F$), as set by the high Fermi energy, E_F, does not allow us to make a decisive distinction between them and the Majorana zero-energy states[47]. Therefore, while the observation of ZBC peaks at the vortex cores may indicate topological superconductivity,

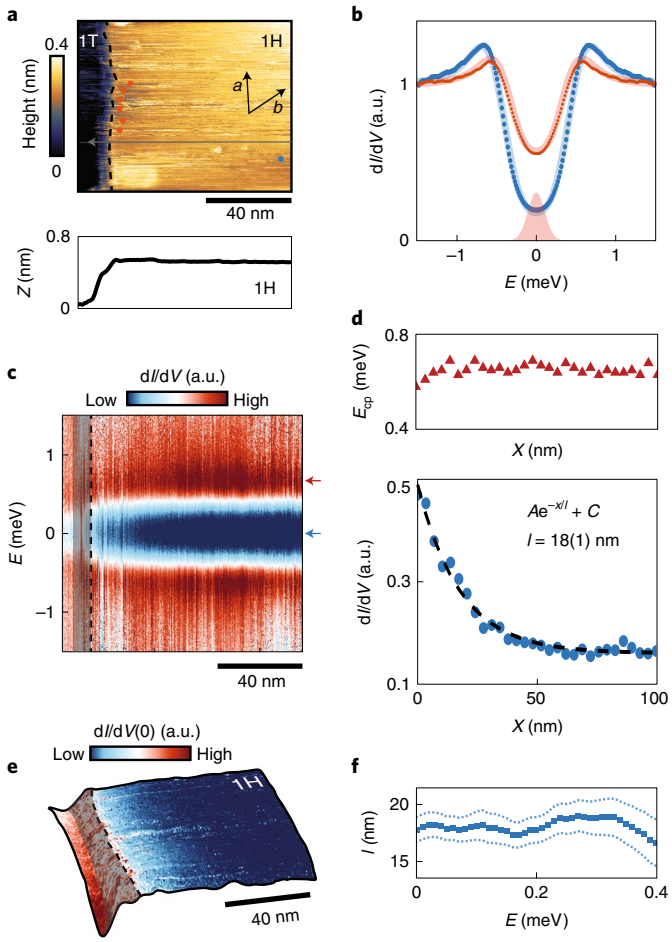

Fig. 2 | Spectroscopic mapping of the dispersing edge mode on 1H step edges. a, Topography of a step edge (dashed black line) between the top 1H and the bottom 1T terraces. Bottom: single 1H-layer height profile of the step edge. **b**, The d*I*/d*V* spectra measured far away from (blue circle) and close to (red circle) the 1H step edge (locations marked in blue in **a** and those averaged over the red circles, respectively), showing increased in-gap DOS near the step edge. The corresponding fits to a BCS with offset and a BCS with offset and a Gaussian profile are shown in pale blue and pale red line, respectively. The Gaussian profile obtained from the fit is shown in filled pale red (Supplementary Fig. 7). **c**, Spatially resolved and energy-resolved d*I*/d*V* across the step edge (dashed line) measured along the grey arrow in **a**. **d**, Top: spatial dependence of the energy of the coherence peaks, E_{cp} (triangles), extracted from **c**. Bottom: ZBC profile evolving away from the step edge at $X = 0$ nm (circles). An exponential fit to the d*I*/d*V* profile (dashed line) finds a localization length of 18(1) nm. **e**, Spatially resolved ZBC d*I*/d*V* map (false colour) overlaid on the topography. **f**, Localization length of the edge mode (l), extracted from exponential fits as in **d**, for several bias energies within the SC gap (blue squares with 95% confidence interval of the fit plotted in dotted lines). Scanning parameters: $V_{set} = 1.5$ mV; $I_{set} = 50$ pA; $V_{a.c.} = 50$ μV; $f = 773$ Hz.

it alone does not provide sufficient evidence for the non-trivial topological nature.

To further investigate the topological nature of the the superconducting state of 4Hb-TaS_2, we explored the spectroscopic properties across the 1H-layer boundaries provided by both 1H and 1T step-edge terminations, since a 2D topological superconductor is expected to carry 1D Majorana modes on its boundaries[13,14]. We first examine the step-edge-terminated 1H layer, as shown in Fig. 2a. Its orientation is roughly along the CDW lattice direction on the 1T layer below it. The d*I*/d*V* spectra measured on the 1H layer at the step-edge boundary and far away from it are shown in Fig. 2b. Far from the step edge (blue circle), we find the soft superconducting gap described above. In contrast, the spectra measured close to the step edge (red circle) show a much shallower suppression of DOS.

We fit the spectra measured around the 1H step edge to a combined model of BCS with a constant offset and a spatially varying Gaussian profile signifying in-gap edge mode contribution to the DOS, as shown in Fig. 2b (Supplementary Fig. 8d). The fit near the edge is in excellent agreement with the data, yielding a somewhat reduced $\Delta \approx 0.33$ meV and a finite value of the Gaussian amplitude relative to the normal-state conductance, namely, $A \approx 30\%$. The fit indicates that the increased in-gap DOS cannot be attributed to the slight suppression in the gap size close to the edge, which may indeed occur at terminations of 2D superconductors (Supplementary Sections 6 and 7). It, thus, signifies the existence of the in-gap edge mode centred around the zero bias.

The spatial profile of the edge mode is seen through the continuous evolution of the spectra, on approaching the step edge in Fig. 2c. The size of the gap—as captured by the energy of the coherence peaks, E_{cp} (Fig. 2d, top), as well as by the detailed fitting to a BCS spectrum with added in-gap Gaussian peak (Supplementary Fig. 10)—hardly changes on approaching the step edge, apart from a slight reduction within a few nanometres from the step edge. In contrast, the in-gap DOS significantly substantially increases over a much longer distance from the step edge (Fig. 2d, bottom). The spatial distribution of the increasing ZBC at distance x from the step edge fits an exponentially localized profile, namely, $Ae^{-x/l}$, above the uniform bulk value with a localization length of $l \approx 18$ nm (Fig. 2d; Supplementary Fig. 11, dashed line). This value is comparable to the coherence length, $\xi \approx 21$ nm, which is extracted from the vortex core profiles (Supplementary Fig. 6a). The exponential localization of the edge mode remains fairly constant across the superconducting gap, as shown in Fig. 2f (Supplementary Figs. 8 and 9), signifying that the edge mode disperses in energy within the superconducting gap. The observed increased ZBC runs all along the rather irregular 1H step edges, as shown in Fig. 2e (Supplementary Fig. 11). It vanishes together with superconductivity when the temperature or magnetic field is raised above their respective critical values (Supplementary Fig. 13), marking that the origin of the edge mode lies in the nature of the superconducting state in the exposed 1H-TaS_2 layer. On the 1T layer residing below the 1H step edge, we find a slight suppression in the DOS (Fig. 2c, left, and Supplementary Fig. 12).

We now show that the edge mode imaged on the boundaries of the 1H-TaS_2 layers is crucially influenced by the adjacent 1T-TaS_2 layer configuration. We investigate 1H layers just below the 1T step edges, providing a boundary between surface-exposed and 1T-encapsulated 1H layers, as shown in Fig. 3a. Since 4Hb-TaS_2 exhibits bulk superconductivity[37], we expect the 1H layer to remain superconducting throughout. Indeed, we commonly image portions of the vortex cores extruding beyond the top 1T-layer termination (Fig. 3b), signifying 1H-TaS_2 superconductivity continues well into the 1T-encapsulated parts. Nevertheless, when we map the ZBC at the boundary of the 1H crater, we clearly image the presence of an edge mode running along it, as shown in Fig. 3c (Supplementary Fig. 14). As before, the increased in-gap DOS cannot be accounted by the negligible reduction in the superconducting gap size (Fig. 3d). The detection of the edge mode within the 1H layer beneath the 1T step edge suggests that a topological phase transition occurs between the exposed 1H layers and the 1T-encapsulated ones.

The last spectroscopic characterization of the edge mode is obtained by following its spatial profile along the crater's varying boundary. We map the ZBC (Fig. 3e) both under a step edge aligned with the 1T CDW pattern (CDW'', red arrow) and the one aligned with the zigzag 1T termination (ZZ', blue arrow). Both show exponentially localized ZBC profile (Fig. 3f). The crystallographic

orientation of the CDW'' 1T step edge is equivalent to that of the 1H step edge discussed in Fig. 2; indeed, both show similar localization length, namely, $l \approx 18$ nm. From this, we deduce that the edge mode characteristics are insensitive to details of the crystallographic step edge and the local potential induced by it. In contrast, the mode along the zigzag 1T edges is about 30% narrower ($l \approx 13$ nm). We compile the localization length data extracted from nine different spectroscopic mappings, as shown in Fig. 3g (additional linecuts are shown in Supplementary Figs. 14–19). We find remarkable consistency among the edge modes mapped along distinct but crystallographically equivalent directions (red and blue symbols, each related by the C_6 rotation), among distinct fields of view (tagged versus asterisked) and among 1H versus 1T terminations (triangular versus circular symbols, respectively). The observed anisotropy of the localization lengths together with the slight anisotropy of the imaged vortex cores suggest an anisotropic gap structure, commonly signifying nodal superconductivity.

We summarize the spectroscopic observations that we have obtained on 4Hb-TaS_2 that support a topological nodal superconducting state. (1) Exposed 1H-TaS_2 layers host exponentially localized edge modes on their crystallographic boundaries that have no trace within the normal state. (2) A similar mode is found on superconducting 1H-TaS_2 layers, at the boundaries between 1T-encapsulated and exposed regions of the same layer. (3) Both edge mode and vortex cores display anisotropic localization length. (4) Vortices exhibit ZBC peaks at their cores. (5) A spatially uniform residual DOS is observed within the superconducting gap throughout the 1H-TaS_2 surface. (6) Observation of the edge mode at the exposed versus 1T-encapsulated boundary further signifies that the topological classification is affected by the configuration of the adjacent 1T layers.

Several theoretical models have considered various realizations of topological superconducting states in TMDs[26–33]. They do not seem to capture all the aspects of our spectroscopic observations, though it very well may be that certain modifications in them will adequately adopt their phenomenology. Here, however, we propose a simple model for topological superconductivity in which on-site cross-orbital pairing is favoured over a standard *s*-wave-like paring. Cross-orbital pairing requires mirror symmetry breaking, and yields a nodal-point Weyl-like topological superconducting state. The detected anisotropic edge modes are, thus, analogous to Fermi-arc boundary modes in topological nodal-point semimetals. As shown below, the model captures all the aspects of our data.

We, thus, turn to describe our model of the inter-orbital pairing state in 4Hb-TaS_2 (more details are provided in Supplementary Section 14 and ref. [34]). We construct a low-energy tight-binding model[48] for the minimal basis set of the three 4*d* orbitals that mainly contribute to the Fermi surface: d_{z^2}, d_{xy} and $d_{x^2-y^2}$ (Fig. 4a; yellow, red and blue, respectively). The resulting band structure, including spin–orbit coupling, plotted along the high-symmetry lines (Fig. 4b), has states at the Fermi energy with mixed orbital texture, depicted by the abovementioned colours. Typically, *s*-wave Cooper pairing, Δ_S, is assumed to be dominant among states with the same orbital texture, which necessitates pairing of singlet spin states. However, system symmetry also permits cross-orbital pairing, Δ_X, characterized by an odd superposition of orbital states even with triplet spin states[38–40]. The intra- and cross-orbital pairing channels compete; when both are comparable, nodal superconductivity is induced, as depicted in Fig. 4c. We, thus, attribute the residual DOS that offsets the BCS-type spectrum (Fig. 1f) to the in-gap nodal states. In ref. [34], it is shown that electron interactions, which are strong in TMD compounds and their effects are abundant, will promote cross-orbital pairing over intra-orbital superconductivity, as crossed orbitals will minimize the on-site charge overlap (Fig. 4a).

The transition from a fully gapped *s*-wave pairing to a nodal-point triplet pairing constitutes a topological phase transition. Our theoretical calculation for the 4Hb-TaS_2 system shows that the nodal-point superconducting state is characterized by six pairs of non-degenerate Dirac bands across the 2D Brillouin zone, as shown in Fig. 4d. These in-gap Dirac bands are singly degenerate and possess well-defined chirality[14,39,40] of opposite signs among time-reversed partners, akin to Weyl bands in a topological semimetal. The separation of the Dirac nodes, as visualized in Fig. 4e, is given by $b = \pm\sqrt{\Delta_X - \Delta_S}/v_F$. The vanishingly small in-gap DOS within an otherwise gapped spectrum does not notably degrade the isotropic structure of vortex cores (Fig. 1g). However, when the bulk chiral bands are projected to an edge, they induce a corresponding topological edge mode, akin to Fermi-arc modes on the boundaries of a Weyl semimetal. In the edge-projected 1D Brillouin zone, the edge mode spans all the momenta between the projected pairs of Dirac nodes with opposite chirality, as shown for a zigzag edge in Fig. 4f (Supplementary Fig. 25).

These edge modes are the ones detected in our experiment at the various 1D boundaries of the 1H layer. In particular, cross-orbital pairing reveals the origin of the edge mode at the boundary between the exposed and 1T-encapsulated 1H layers, signifying a topological phase transition that occurs across it. According to our model, the origin of this transition lies in the mirror-symmetry-breaking nature of the inter-orbital pairing term, Δ_X. Accordingly, the 1T-encapsulated superconducting 1H layer, representative of bulk behaviour, exhibits a rather symmetric electronic environment (Fig. 1a), whereas the exposed 1H layers are mirror symmetry broken (Supplementary Section 14.2). This is greatly amplified by the strong interaction between the 1T and 1H layers. Our ab initio calculations find a substantial charge (and spin) transfer from the CDW-localized state on the 1T layer to the adjacent 1H layer where it remains rather localized (Supplementary Fig. 22), as indeed captured in our measurements (Fig. 1d). The charge transfer induces a local dipole field between the two layers. Its effect on the 1H layer is balanced in the symmetrically encapsulated case, but sustains in the exposed 1H layer that only has a 1T layer beneath it.

Fig. 3 | Spectroscopic mapping of the anisotropic edge mode below 1T step edges. a, Topography of a crater in the 1T termination of 4Hb-TaS_2, exposing the 1H layer at its bottom (1T CDW directions are marked by arrows). Bottom: height profile across the single-layer step edges extracted along the white dotted line. **b**, Spatially resolved ZBC d*I*/d*V* map (false colour) measured with an out-of-plane field (B_z) of 50 mT, in box 'b' in **a**, overlaid on top of the topography, showing a partially exposed vortex on the 1H surface. Inset shows a large-scale zoomed-out map of the vortex lattice in the same region. **c**, The d*I*/d*V* linecut measured along the dashed line marked by 'c' in **a**. **d**, The spatial dependence of the energy of the coherence peaks (E_{cp}), extracted from **c**. **e**, Spatially resolved ZBC d*I*/d*V* map, measured in box 'e' in **a**, showing a continuous edge mode under the 1T step edge (marked by the dashed line). **f**, The ZBC profile, evolving away from the step edge extracted perpendicular to the zigzag edge and the one aligned with the CDW direction (labelled as ZZ' and CDW'', respectively), as indicated by the blue and red arrows in **e**. The ZBC profile labelled ZZ'' (black symbols, marked as 'c' in **a**) is extracted from the step edge along a distinct direction that is crystallographically equivalent to the zigzag edge ZZ'. Localization lengths are extracted through exponential fits (dashed lines). **g**, Collection of fitted localization lengths of nine spectroscopic mappings. Prime symbols denote profiles extracted from the same field of view shown in **a**, so their relative orientation is known. Asterisks indicate profiles that are extracted from a remote field of view. The solid line depicts the angular dependence of a maximally localized mode based on a simplified model. Scanning parameters for **b** and **e**: parking bias (V_{set}) = 2 mV; current (I_{set}) = 100 pA; a.c. probe voltage ($V_{a.c.}$) = 100 μV; frequency (f) = 773 Hz.

The momentum-space distribution of in-gap nodal points, which induces the edge mode, also entails its anisotropic nature. Both mode dispersion and localization length depend on the crystallographic direction to which it is projected. Projection onto the zigzag edge along Γ–M yields an electron–hole symmetric pair of dispersing modes among the doubly degenerate projected Dirac

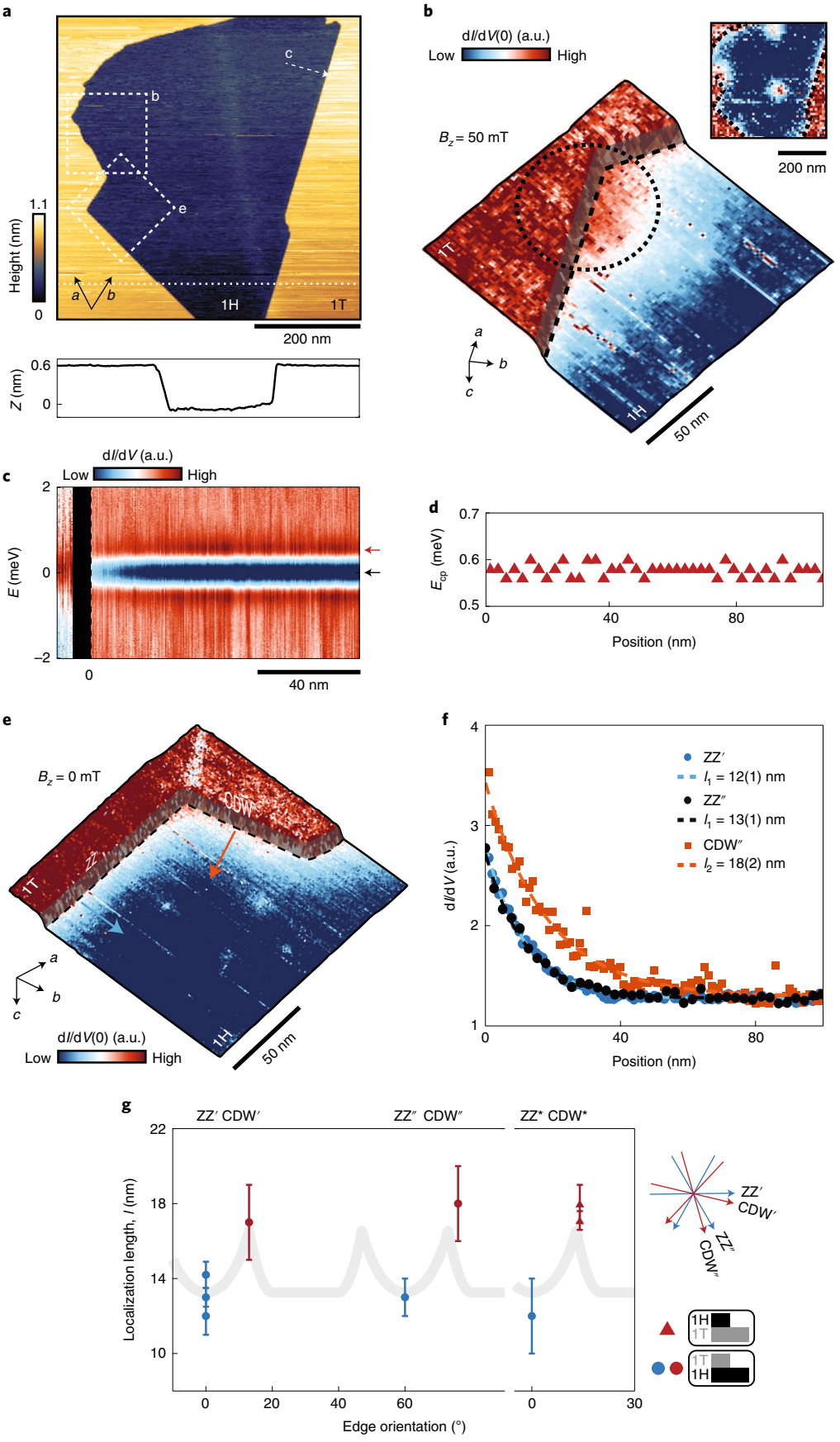

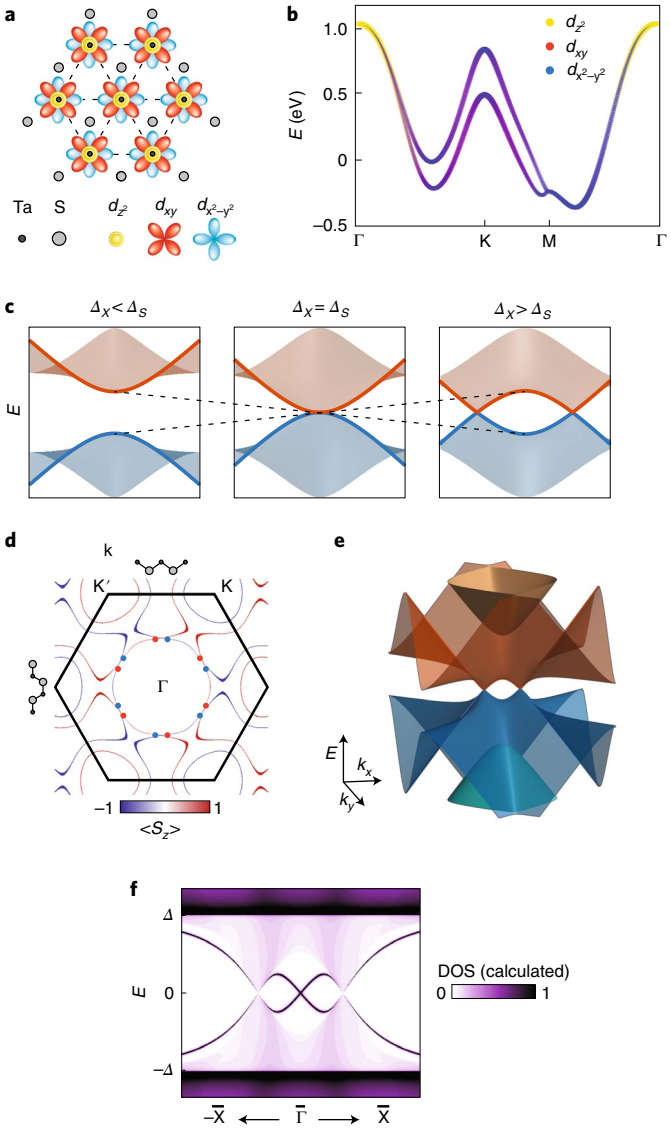

Fig. 4 | Topological nodal superconductivity induced by inter-orbital pairing. a, Schematic of the various *d* orbitals of Ta decorating the 1H-TaS_2 lattice. **b**, Calculated band structure of 1H-TaS_2 with different orbital contributions encoded in colour. **c**, Schematic of a topological phase transition with increasing ratio of inter- and intra-orbital pairing amplitudes, Δ_X/Δ_S. **d**, Calculated Fermi surface of 1H-TaS_2. The chirality of the topological nodal points is shown in red and blue circles. **e**, Schematic showing a pair of topological nodal points for $\Delta_X > \Delta_S$. **f**, Calculated DOS along the zigzag edge, showing dispersing helical Majorana edge modes.

nodes (Fig. 4f). Its crossing point at $\bar{\Gamma}$ is protected by a combined mirror and time-reversal operation, M_xT. As the projection deviates from Γ−M onto arbitrary directions, we find a singly degenerate non-dispersing mode stretching between the edge-projected nodes (as illustrated in Supplementary Fig. 28; Supplementary Fig. 25 provides additional details). The projection of the 12 nodal points onto distinct crystallographic directions gives rise to a complex angular dependence. The exact values depend on many parameters such as the strength of the surface Rashba spin–orbit energy, which affects the nodal points distribution in the Brillouin zone (Supplementary Section 14.4). Our experimental energy resolution does not allow to discern the details of the varying dispersion of the edge modes along various crystallographic directions. However, the anisotropic nature of localization length that we map along various directions is clearly exhibited by our model. The overall order of magnitude discrepancy in the values determined using the model can be attributed to the renormalized Fermi velocity[45] that the model neglects (Supplementary Section 14.5).

The angular dependence of the localization length is captured by a native model for the maximally localized edge mode profile based on the nodal gap structure. We assume that angular anisotropy is dominated by the maximum bulk-gap value for a given projection direction. We again use the relation $\xi_{\min} \approx \hbar v_F/\Delta_{\max}(\theta)$, where $\Delta_{\max}$ is chosen as the maximal inter-nodal gap when two time-reversed pairs of nodal bands from opposite sides of the Brillouin zone are overlaid and displaced by the relative projection angle θ (Supplementary Fig. 28). The resulting angular dependence (Fig. 3g, solid line) captures remarkably well the anisotropic localization trend found in our experiment. It further elucidates that under this simplified model, the edge-mode anisotropy around the zigzag direction is restricted by the nodal-point separation to an angular interval over which the projected pairs of bulk nodal points overlap.

Finally, we note that our measurements cannot determine whether the topological superconductivity observed on the surface is time-reversal symmetric or not. Our ab initio calculations find that the charge transfer from the 1T to 1H layer is also accompanied by the transfer of magnetic moment, which may very well give rise to magnetically ordered states once the magnetic moments are embedded within the metallic 1H layer (Supplementary Section 13). Indeed, enhanced muon relaxation was reported to concurrently onset below the superconducting transition[37]. Our theoretical calculations show that adding a time-reversal symmetry-breaking term does not eliminate the edge modes from any of the edge directions but only slightly affects their dispersion in a way that cannot be distinguished by our spectroscopic measurements (Supplementary Information provides more details). Spontaneous time-reversal symmetry breaking may support other origins for the observed topological superconducting state[18] and should thus be further investigated.

Online content

Any methods, additional references, Nature Research reporting summaries, source data, extended data, supplementary information, acknowledgements, peer review information; details of author contributions and competing interests; and statements of data and code availability are available at https://doi.org/10.1038/s41567-021-01376-z.

Received: 14 July 2021; Accepted: 3 September 2021;
Published online: 25 October 2021

References

1. Kitaev, A. Y. Fault-tolerant quantum computation by anyons. *Ann. Phys.* **303**, 2–30 (2003).
2. Nayak, C., Simon, S. H., Stern, A., Freedman, M. & Das Sarma, S. Non-Abelian anyons and topological quantum computation. *Rev. Mod. Phys.* **80**, 1083 (2008).
3. Lutchyn, R. M. et al. Majorana zero modes in superconductor–semiconductor heterostructures. *Nat. Rev. Mater.* **3**, 52–68 (2018).
4. Nadj-Perge, S. et al. Observation of Majorana fermions in ferromagnetic atomic chains on a superconductor. *Science* **346**, 602–607 (2014).
5. Jäck, B. et al. Observation of a Majorana zero mode in a topologically protected edge channel. *Science* **364**, 1255–1259 (2019).
6. Fornieri, A. et al. Evidence of topological superconductivity in planar Josephson junctions. *Nature* **569**, 89–92 (2019).
7. Ren, H. et al. Topological superconductivity in a phase-controlled Josephson junction. *Nature* **569**, 93–98 (2019).
8. Yin, J.-X. et al. Observation of a robust zero-energy bound state in iron-based superconductor Fe(Te,Se). *Nat. Phys.* **11**, 543–546 (2015).
9. Kong, L. et al. Half-integer level shift of vortex bound states in an iron-based superconductor. *Nat. Phys.* **15**, 1181–1187 (2019).
10. Zhu, S. et al. Nearly quantized conductance plateau of vortex zero mode in an iron-based superconductor. *Science* **367**, 189–192 (2019).

11. Liu, Q. et al. Robust and clean Majorana zero mode in the vortex core of high-temperature superconductor ($Li_{0.84}Fe_{0.16}$) OHFeSe. *Phys. Rev. X* **8**, 041056 (2018).
12. Chen, C. et al. Atomic line defects and zero-energy end states in monolayer Fe(Te,Se) high-temperature superconductors. *Nat. Phys.* **16**, 536–540 (2020).
13. Qi, X.-L. & Zhang, S.-C. Topological insulators and superconductors. *Rev. Mod. Phys.* **83**, 1057 (2011).
14. Schnyder, A. P. & Brydon, P. M. R. Topological surface states in nodal superconductors. *J. Phys. Condens. Matter* **27**, 243201 (2015).
15. Sato, M. & Ando, Y. Topological superconductors: a review. *Rep. Prog. Phys.* **80**, 076501 (2017).
16. Ménard, G. C. et al. Two-dimensional topological superconductivity in Pb/Co/Si(111). *Nat. Commun.* **8**, 2040 (2017).
17. Palacio-Morales, A. et al. Atomic-scale interface engineering of Majorana edge modes in a 2D magnet-superconductor hybrid system. *Sci. Adv.* **5**, eaav6600 (2019).
18. Kezilebieke, S. et al. Topological superconductivity in a van der Waals heterostructure. *Nature* **588**, 424–428 (2020).
19. Yuan, Y. et al. Evidence of anisotropic Majorana bound states in 2M-WS_2. *Nat. Phys.* **15**, 1046–1051 (2019).
20. Jiao, L. et al. Chiral superconductivity in heavy-fermion metal UTe_2. *Nature* **579**, 523–527 (2020).
21. Ye, J. T. et al. Superconducting dome in a gate-tuned band insulator. *Science* **338**, 1193–1196 (2012).
22. Xi, X. et al. Ising pairing in superconducting $NbSe_2$ atomic layers. *Nat. Phys.* **12**, 139–143 (2016).
23. de la Barrera, S. C. et al. Tuning Ising superconductivity with layer and spin–orbit coupling in two-dimensional transition-metal dichalcogenides. *Nat. Commun.* **9**, 1427 (2018).
24. Sajadi, E. et al. Gate-induced superconductivity in a monolayer topological insulator. *Science* **362**, 922–925 (2018).
25. Fatemi, V. et al. Electrically tunable low-density superconductivity in a monolayer topological insulator. *Science* **362**, 926–929 (2018).
26. Yuan, N. F., Mak, K. F. & Law, K. T. Possible topological superconducting phases of MoS_2. *Phys. Rev. Lett.* **113**, 097001 (2014).
27. Zhou, B. T., Yuan, N. F., Jiang, H. L. & Law, K. T. Ising superconductivity and Majorana fermions in transition-metal dichalcogenides. *Phys. Rev. B* **93**, 180501 (2016).
28. Hsu, Y.-T., Vaezi, A., Fischer, M. H. & Kim, E.-A. Topological superconductivity in monolayer transition metal dichalcogenides. *Nat. Commun.* **8**, 14985 (2017).
29. He, W.-Y. et al. Magnetic field driven nodal topological superconductivity in monolayer transition metal dichalcogenides. *Commun. Phys.* **1**, 40 (2018).
30. Fischer, M. H., Sigrist, M. & Agterberg, D. F. Superconductivity without inversion and time-reversal symmetries. *Phys. Rev. Lett.* **121**, 157003 (2018).
31. Hsu, Y. T., Cole, W. S., Zhang, R. X. & Sau, J. D. Inversion-protected higher-order topological superconductivity in monolayer WTe_2. *Phys. Rev. Lett.* **125**, 097001 (2020).
32. Kanasugi, S. & Yanase, Y. Multiple odd-parity superconducting phases in bilayer transition metal dichalcogenides. *Phys. Rev. B* **102**, 094507 (2020).
33. Shaffer, D., Kang, J., Burnell, F. J. & Fernandes, R. M. Crystalline nodal topological superconductivity and Bogolyubov Fermi surfaces in monolayer $NbSe_2$. *Phys. Rev. B* **101**, 224503 (2020).
34. Margalit, G., Berg, E. & Oreg, Y. Theory of multi-orbital topological superconductivity in transition metal dichalcogenides. *Ann. Phys*. https://doi.org/10.1016/j.aop.2021.168561 (in the press).
35. Geim, A. K. & Grigorieva, I. V. Van der Waals heterostructures. *Nature* **499**, 419–425 (2013).
36. Law, K. T. & Lee, P. A. 1T-TaS_2 as a quantum spin liquid. *Proc. Natl Acad. Sci. USA* **114**, 6996–7000 (2017).
37. Ribak, A. et al. Chiral superconductivity in the alternate stacking compound 4Hb-TaS_2. *Sci. Adv.* **6**, eaax9480 (2020).
38. Gao, Y., Su, W.-P. & Zhu, J.-X. Interorbital pairing and its physical consequences for iron pnictide superconductors. *Phys. Rev. B* **81**, 104504 (2010).
39. Wang, F. & Lee, D.-H. Topological relation between bulk gap nodes and surface bound states: application to iron-based superconductors. *Phys. Rev. B* **86**, 094512 (2012).
40. Fukaya, Y. et al. Interorbital topological superconductivity in spin-orbit coupled superconductors with inversion symmetry breaking. *Phys. Rev. B* **97**, 174522 (2018).
41. Di Salvo, F. J., Bagley, B. G., Voorhoeve, J. M. & Waszczak, J. V. Preparation and properties of a new polytype of tantalum disulfide (4Hb-TaS_2). *J. Phys. Chem. Solids* **34**, 1357–1362 (1973).
42. Tanaka, M. et al. Study of 4Hb-TaS_2 and graphite intercalation compound by STM/STS. *J. Microsc.* **152**, 183–192 (1988).
43. Kim, J. J. & Olin, H. Atomic- and electronic-structure study on the layers of 4Hb-TaS_2 prepared by a layer-by-layer etching technique. *Phys. Rev. B* **52**, R14388(R) (1995).
44. Fujisawa, Y. et al. Superposition of $\sqrt{13} \times \sqrt{13}$ and 3×3 supermodulations in TaS_2 probed by scanning tunneling microscopy. *J. Phys. Conf. Ser.* **969**, 012053 (2018).
45. Wijayaratne, K. et al. Spectroscopic signature of moment-dependent electron–phonon coupling in 2H-TaS_2. *J. Mater. Chem. C* **5**, 11310 (2017).
46. Reiner, J. et al. Spectroscopic visualization of a robust electronic response of semiconducting nanowires to deposition of superconducting islands. *Phys. Rev. X* **10**, 011002 (2020).
47. Hess, H. F., Robinson, R. B., Dynes, R. C., Valles, J. M. & Waszczak, J. V. Scanning-tunneling-microscope observation of the Abrikosov flux lattice and the density of states near and inside a fluxoid. *Phys. Rev. Lett.* **62**, 214 (1989).
48. Möckli, D. & Khodas, M. Robust parity-mixed superconductivity in disordered monolayer transition metal dichalcogenides. *Phys. Rev. B* **98**, 144518 (2018).

Methods

Sample growth. High-quality single crystals of 4Hb-TaS_2 were prepared using the chemical vapour transport method. Appropriate amounts of Ta and S were ground and mixed with a small amount of Se (1% of the S amount). The powder was sealed in a quartz ampoule, and a small amount of iodine was added as a transport agent. The ampoule was placed in a three-zone furnace such that the powder is in the hot zone. After 30 days, single crystals with a typical size of 5.0 mm × 5.0 mm × 0.1 mm grew in the cold zone of the furnace.

STM measurements. The 4Hb-TaS_2 single crystals were cleaved in the STM load lock under ultrahigh-vacuum conditions and at room temperature. The STM measurements were performed using commercial Pt–Ir tips. These tips were characterized on a freshly prepared Cu(111) single crystal. This process ensured a stable tip with reproducible results. All the dI/dV measurements were taken using standard lock-in techniques.

Density functional theory calculations. We performed the density functional theory calculation in the framework of the generalized gradient approximation[49] with the Vienna ab initio simulation package[50]. We employed the PBE-D2 method to describe the van der Waals interaction[51]. We included the spin–orbit coupling interaction in all the calculations. The 4Hb structure with a $\sqrt{13} \times \sqrt{13}$ supercell was used for the CDW-reconstructed structure. Full geometry optimization was performed until the Hellmann–Feynman force acting on each atom became smaller than 0.01 eV Å^{-1}.

Data availability

The data needed to reproduce the main text figures are available on Zenodo (https://doi.org/10.5281/zenodo.5229526).

Code availability

The codes used in theoretical simulations and calculations are available from the corresponding authors upon reasonable request.

References

49. Perdew, J. P., Burke, K. & Ernzerhof, M. Generalized gradient approximation made simple. *Phys. Rev. Lett.* **77**, 3865 (1996).
50. Kresse, G. & Joubert, D. From ultrasoft pseudopotentials to the projector augmented-wave method. *Phys. Rev. B* **59**, 1758 (1999).
51. Grimme, S. Semiempirical GGA-type density functional constructed with a long-range dispersion correction. *J. Comput. Chem.* **27**, 1787–1799 (2006).

Acknowledgements

N.A., H.B. and B.Y acknowledge the German-Israeli Foundation for Scientific Research and Development (GIF grant no. I-1364-303.7/2016). H.B. and N.A. acknowledge the European Research Council (ERC, project no. TOPO NW). B.Y. acknowledges financial support by the European Research Council (ERC Consolidator Grant, no. 815869), the Israel Science Foundation (ISF nos. 1251/19, 3520/20 and 2932/21) and the Willner Family Leadership Institute for the Weizmann Institute of Science, the Benoziyo Endowment Fund for the Advancement of Science, the Ruth and Herman Albert Scholars Program for New Scientists, and the Israel Science Foundation (ISF 1251/19). G.A.F. gratefully acknowledges partial support from the National Science Foundation through NSF grant nos. DMR-1720595 and DMR-1949701. Y.O. acknowledges partial support through the ERC under the European Union's Horizon 2020 research and innovation programme (grant agreement LEGOTOP no. 788715), the ISF Quantum Science and Technology (2074/19), the BSF and NSF (2018643), and the CRC/Transregio 183. A.K. acknowledges the Israel Science Foundation (ISF 320/17).

Author contributions

A.K.N., A.S. and Y.R. acquired and analysed the data. A.K., N.A. and H.B. conceived the experiments. J.K. and B.Y. calculated the ab initio model. G.M., G.A.F., B.Y. and Y.O. calculated the theoretical model. I.F., A.A. and A.K. grew the material. A.K.N., N.A. and H.B. wrote the manuscript with substantial contributions from all the authors.

Competing interests

The authors declare no competing interests.

Additional information

Supplementary information The online version contains supplementary material available at https://doi.org/10.1038/s41567-021-01376-z.

Correspondence and requests for materials should be addressed to Nurit Avraham or Haim Beidenkopf.

Peer review information *Nature Physics* thanks the anonymous reviewer for their contribution to the peer review of this work**Reprints and permissions information** is available at www.nature.com/reprints.